Inorganic Chemistry
Article
pubs.acs.org/IC

Crystal Structure, Phase Transitions, and Magnetic Properties of Iridium Perovskites Sr_2MIrO_6 (M = Ni, Zn)

P. Kayser,*[†] M. J. Martínez-Lope,[†] J. A. Alonso,[†] M. Retuerto,[‡] M. Croft,[§] A. Ignatov,[§] and M. T. Fernández-Díaz[#]

[†]Instituto de Ciencia de Materiales de Madrid, C.S.I.C., Cantoblanco E-28049 Madrid, Spain

[‡]Department of Chemistry and Chemical Biology, [§]Department of Physics and Astronomy, Rutgers, the State University of New Jersey, 610 Taylor Road, Piscataway, New Jersey 08854-808, United States

[#]Institut Laue Langevin, BP 156X, Grenoble, F-38042, France

Supporting Information

ABSTRACT: Double perovskites containing Ir^{6+}/Ir^{5+} with formula Sr_2MIrO_6 (M = Ni, Zn) have been synthesized under high oxygen pressure conditions. Their crystal structures have been studied by X-ray and neutron powder diffraction at room temperature (RT) and 2 K. At RT, these oxides crystallize in the monoclinic space group $P2_1/n$ with unit-cell parameters $a \approx \sqrt{2}a_0$, $b \approx \sqrt{2}a_0$, and $c \approx 2a_0$, and $\beta \approx 90°$. The thermal evolution of the structure of the Ni-containing compound shows the presence of two phase transition in the 373−673 K interval following the sequence $P2_1/n \rightarrow I4/m \rightarrow Fm\bar{3}m$. These materials have also been characterized by magnetic measurements, suggesting the onset of antiferromagnetic interactions at T_N = 58 and 46 K, for M = Ni, Zn, respectively. X-ray absorption spectroscopy sheds light on the oxidation states of M and Ir ions within these double perovskites.

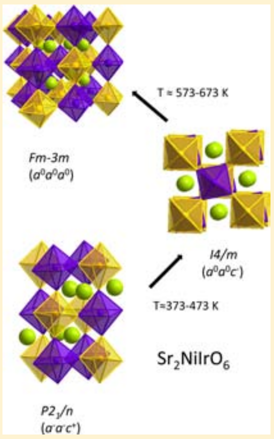

■ INTRODUCTION

Recently, the study of iridium-based oxides has attracted a lot of attention in materials science, since elements with 4d and particularly 5d electrons are expected to present unusual electronic structures due to their characteristic spin−orbit coupling.[1] 4d and 5d orbitals, especially in compounds as layered oxides such as Sr_2RuO_4, Sr_2RhO_4, Sr_2IrO_4,[2] and $NaIrO_3$,[3] are more spatially extended than the 3d orbital, and thus the Coulomb interaction is typically weaker, leading to a greater level of splitting of the crystal field and an increment of their sensitivity to lattice distortions. In perovskite oxides, where the 4d and 5d transition metal cations are located inside oxygen octahedra, in addition to the crystal field splitting also relevant is the spin−orbit coupling that results from the large atomic number of heavy transition elements. A large spin−orbit coupling modifies the relative energy scales as its level approaches the energy of the Coulomb interactions. This phenomenon may lead to the appearance of novel phases with unconventional electronic structures.

For large enough spin−orbit coupling, the new effective spin states lead to a great deal of novel Mott insulating states, possible spin liquids in the hyperkagome lattice, orbital-oriented exchange coupling in Kitaev-type models, topological Mott insulators, and topological magnetic insulators with axionic excitations.[4] In particular, pyrochlore iridates have been broadly studied because novel topological phases have been theoretically proposed due to their geometrical frustration.[5] Perovskite iridates, on the other hand, show a wide range of properties going from metal conductivity and Pauli paramagnetism in $SrIrO_3$[6,7] to weak ferromagnetism, orbital magnetism, and spin−orbit effects in $BaIrO_3$.[8−10] Morever, the introduction of a 3d magnetic cation in the B sublattice in a double perovskite could introduce even new and interesting properties.

In the last years, double perovskites of stoichiometry $Sr_2BB'O_6$ (B = 3d transition metals; B′= 4d or 5d transition metals or p-block elements: Mo, Re, W, U, Sb, Te, Ru) have been widely studied due to their intriguing physical properties as half-metals with colossal magnetoresistance (Sr_2FeMoO_6, Sr_2FeReO_6)[11] or magnetic order far above room temperature (Sr_2CrOsO_6, Sr_2CrReO_6).[12,13] However, analogous oxides with perovskite or perovskite-like structure containing iridium have been much less explored. The stabilization of Ir^{5+} and Ir^{6+} is especially interesting since Ir^{5+}−O and Ir^{6+}−O bonds should be among the strongest chemical bonds in an oxygen lattice. The covalency of such chemical bonding is correlated with the values of the magnetic ordering temperature. In fact, it has been theoretically predicted that hypothetical double perovskites

Received: May 9, 2013
Published: September 12, 2013

dx.doi.org/10.1021/ic401161d | *Inorg. Chem.* 2013, 52, 11013−11022

such as Sr_2CrIrO_6 should exhibit the highest T_C ever reported for half-metallic ferromagnets.[14]

Some iridium-based double perovskites, with iridium taking the oxidation states Ir^{5+} and Ir^{6+}, have been previously described in the pioneering work by Demazeau et al.[15] in 1995, where Ir^{6+} is combined with a divalent cation, such as Ca^{2+} and Mg^{2+}. Some years later, several perovskites with Ir^{5+} and a trivalent M^{3+} transition metal (Co and Fe) and rare earths were reported.[16−18] Also the crystal structure, the magnetic and electric properties of some members of the $SrIr_{1-x}M_xO_3$ (M = Fe, Co, Ni, and Zn) solid solution were described by Ilyas Qasim et al.[19] The main motivation of our current research is to explore novel 3d−5d double perovskites containing Ir^{6+}. In this work. we have been able to stabilize for the first time Sr_2MIrO_6 (M = Zn and Ni) under high-oxygen pressure and high temperature (900 °C) conditions. We report a complete study of the crystallographic structure from neutron powder diffraction (NPD) data, complemented with magnetic measurements and X-ray absorption spectroscopy; the magnetic properties of iridium ions in the presence of both diamagnetic Zn cations and magnetic Ni cations will be also discussed.

■ EXPERIMENTAL SECTION

Polycrystalline samples of Sr_2ZnIrO_6 and Sr_2NiIrO_6 were prepared via citrate-nitrate method. Stoichiometric amounts of 0.004 mol of $Sr(NO_3)_2$ (Merck) and 0.002 mol of ZnO (Alfa-Aesar 99.999%) or 0.002 mol of $Ni(NO_3)_2{\cdot}6H_2O$ (Merck), respectively, were dissolved in 100 ml of citric acid aqueous solution (10% w/w) with 1 ml of HNO_3. IrO_2 (Strem 99%) (0.002 mol) was added to this solution and remained in suspension with continuous stirring. This suspension was slowly evaporated leading to organic resins that contain a homogeneous distribution of the involved cations. After evaporation, the resulting resins were dried at 140 °C and then heated at 600 °C in air for 12 h, with a heating rate of 2 °C/min, in order to decompose the organic materials and eliminate the nitrates. Subsequently, annealing treatments in an oxidizing atmosphere were necessary to obtain pure perovskite oxides, with iridium cations taking the oxidation states Ir^{5+} and Ir^{6+}. In both samples, the obtained precursor powders were ground in an agate mortar, placed in alumina boats, and heated in a CARBOLITE tubular furnace at 900 °C in an O_2 flow for 12 h with a heating rate of 3 °C/min. Finally, the samples were reground, introduced in a gold crucible, and heated in a MORRIS RESEARCH furnace at 900 °C (heating rate of 10 °C/min) under 200 bar of oxygen for 48 h.

The reaction progress was followed after each treatment by X-ray diffraction (XRD), using a Bruker-AXS D8 diffractometer (40 kV, 30 mA), controlled by DIFFRAC^{PLUS} software, in Bragg−Brentano reflection geometry with Cu Kα radiation (λ = 1.5418 Å) and a position sensitive detector (PSD). XRD patterns at different temperatures (298, 373, 473, 573, 673, 773, 873, 973, and 1073 K) were also carried out for Sr_2NiIrO_6 oxide using a Panalytical X′Pert PRO theta/2theta diffractometer equipped with a high-temperature chamber (HTK 1200N) and Xenon detector.

To study the crystallographic structures, neutron powder diffraction (NPD) patterns were collected at room temperature at the high-resolution D2B diffractometer (λ = 1.594 Å) of the Institute Laue-Langevin (ILL) in Grenoble. The possible magnetic ordering of the samples at 2 K was studied from NPD diagrams, acquired on the D1B instrument (λ = 2.52 Å). High-temperature NPD data were also collected for M = Ni at D2B at 473, 573, and 873 K to investigate possible phase transitions. The NPD data were refined by the Rietveld method,[20] using the FULLPROF refinement program.[21] A pseudo-Voigt function was chosen to generate the line shape of the diffraction peaks. No regions were excluded in the refinement. The following parameters were refined in the final runs: scale factor, background coefficients, zero-point error, pseudo-Voigt corrected for asymmetry parameters, positional coordinates, and isotropic displacements.

The magnetic properties were studied using a commercial Quantum-Design superconducting quantum interference device (SQUID) magnetometer. The magnetic susceptibility was measured both in zero-field-cooled (ZFC) mode and field-cooled (FC) mode in the $4 \leq T \leq 400$ K range under an applied magnetic field of 0.1 T. Isothermal magnetization curves were obtained for magnetic fields going from −5 to 5 T at 4 and 300 K.

X-ray absorption near edge spectroscopy (XANES) was collected simultaneously in both the transmission and fluorescence mode on powder samples on X-19A beamline at the Brookhaven National Synchrotron Light Source. In order to compare the samples of Sr_2ZnIrO_6 and Sr_2NiIrO_6 with related compounds, Sr_2FeIrO_6 and Sr_2MgIrO_6 oxides were prepared by solid state reactions; the synthesis conditions were reported in refs 15 and 16.

■ RESULTS AND DISCUSSION

Crystal Structure. *Room-Temperature Crystal Structure.* Single-phases of the double perovskites Sr_2NiIrO_6 and Sr_2ZnIrO_6 were obtained as black and well-crystallized powders. Figure 1 shows the XRD patterns, characteristic of perovskite-type structures. Both compounds exhibit superstructure reflections, (011) and (013), due to the rock-salt ordered arrangement of Ni^{2+}/Zn^{2+} and Ir^{6+} cations in B and B′ double perovskite sites combined with the tilting of the BO_6 octahedra. The XRD patterns were fit to the structural model developed from NPD data, described below in a monoclinic unit-cell in the space group $P2_1/n$ (No. 14). The unit-cell parameters are related to a_0 (ideal cubic perovskite $a_0 \approx 3.8$ Å) as $a \approx \sqrt{2}a_0$, $b \approx \sqrt{2}a_0$ and $c \approx 2a_0$, $\beta \approx 90°$.

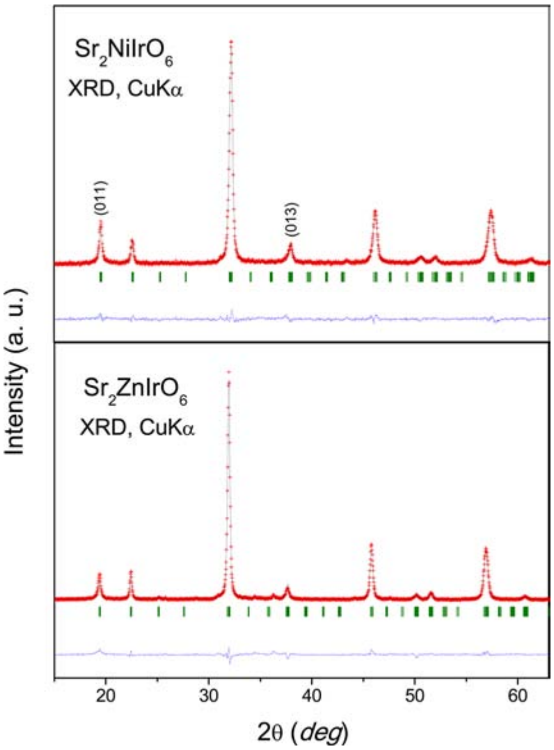

Figure 1. XRD patterns (Cu Kα, λ = 1.5406 Å) for Sr_2MIrO_6 (M = Ni, Zn) oxide.

An accurate structural refinement was carried out from RT high-resolution NPD data using a model described in the monoclinic $P2_1/n$ space group with Sr atoms located at 4e (x y

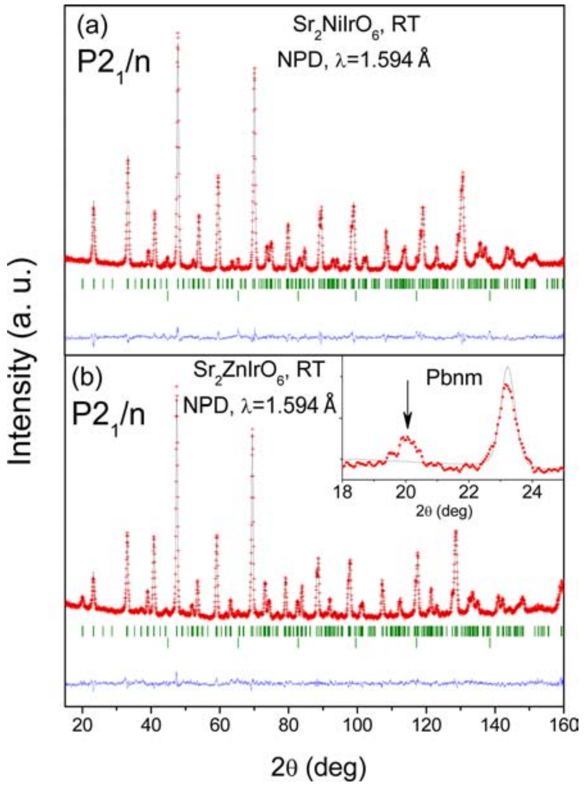

Figure 2. Observed (crosses), calculated (solid line), and difference (bottom) NPD Rietveld profiles for Sr_2MIrO_6 (M = Ni, Zn) at RT, collected at the high flux D2B-ILL diffractometer. The first series of Bragg reflections correspond to the main perovskite phase and the second corresponds to the vanadium from the sample holder.

z) positions, Ni/Zn at 2d (1/2 0 0) positions, Ir at 2c (1/2 0 1/2), and the three types of oxygen atoms at 4e (x y z) sites, which resulted in a satisfactory agreement between the observed and calculated profiles (Figure 2). In a further step, for Sr_2ZnIrO_6 the fit of the neutron diffraction profiles was strongly improved by allowing a small degree of disorder in the Zn vs Ir distribution, which means the refinement of the level of antisite disorder between Zn and Ir cations at both B and B′ sites, resulting in a percentage of long-range ordering of 87% for Sr_2ZnIrO_6. For Sr_2NiIrO_6 a long-range ordering of 92% was determined from XRD data, since the neutron scattering lengths between Ni (1.03 fm) and Ir (1.06 fm) are extremely similar to each other; this value was fixed in the final NPD refinement. Also we have refined the occupancy factors of oxygen atoms, and the results confirm a full stoichiometry for the Sr_2NiIrO_6 sample and the presence of some oxygen vacancies for $Sr_2ZnIrO_{6-\delta}$ ($\delta = 0.13$). After the final refinement, very reasonable fits ($R_I \approx 2.99\%$ for Ni compound and 3.04% for Zn compound) were obtained. Tables 1 and 2 list the most important atomic parameters of the structural refinements and Tables 3 and 4 include the interatomic distances and some selected bond angles for Sr_2NiIrO_6 and Sr_2ZnIrO_6, respectively. Figure 2 illustrates the goodness of the fit for both compounds. An alternative refinement in the *Pbnm* space group, corresponding to a B-site disordered crystal structure, is described in the Supporting Information, including Figure S1. This disordered model was finally discarded. As an irrefutable evidence, the inset of Figure 2b shows the absence of calculated [101] reflection in the *Pbnm* model.

For Sr_2NiIrO_6, the average <Ni−O> and <Ir−O> bond lengths (1.986(12) Å and 1.972(13) Å) are comparable with the sums of Shannon[22] effective radii, if Ni^{3+} and Ir^{5+} are considered. However, the comparison of the Ni−O distances with several examples of Ni-containing perovskites (2.03 Å for Ni^{2+} in $Sr_2Ni(Mo,Re,U)O_6$[23−25] and 1.93−1.96 Å for Ni^{3+}in $RNiO_3$[26]) suggests the presence of both Ni^{2+} and Ni^{3+} cations at the 2d site. On the other hand, reported Ir−O bond lengths are quite structure-dependent, and the typical lengths for octahedral environments are 1.95−1.99 Å for Ir^{5+} and 1.90−1.95 Å for Ir^{6+}.[15,16,27,28] Therefore, the obtained value of 1.972(13) Å in the Sr_2NiIrO_6 double perovskite, comparatively longer than the one reported by Demazeau et al. for Ir^{6+},[15] suggests the presence of iridium cations with mixed penta-/hexavalent state. The shortening of the Ni−O bond distances, compared with the bibliographic Ni^{2+}−O distances, and the larger Ir−O bond distances with respect to the reported Ir^{6+}−O are due to two effects: the B-antisite disorder and the presence of mixed valence. In Sr_2ZnIrO_6, the Ir−O bond length (1.954(9) Å) is almost equal to those reported in Ir^{6+}-containing compounds, and shorter than those in Ir^{5+} oxides,[16] indicating higher content of Ir^{6+}; the average <Zn−O> bond length (2.044(9) Å) is somewhat lower than the sum of the radii given by Shannon (2.14 Å), suggesting a compression of the Zn−O bonds.

It is also interesting to have an insight on the valences of the cations through the calculation of the bond-valences from structural data.[29−31] In the Brown's model,[30] the valence is the sum of the individual bond valences (s_i) for (Ni/Zn)−O and Ir−O bonds. The bond valences are calculated as $s_i = \exp[(r_0 - r_i)/B]$; $B = 0.37$, $r_0 = 1.654$ for the Ni^{2+}−O^{2-} pair; $r_0 = 1.704$ for Zn^{2+}−O^{2-}; $r_0 = 1.916$ for Ir^{5+}−O^{2-}, and $r_0 = 2.118$ for Sr^{2+}−O^{2-} from ref 29. Individual Ni−O, Ir−O, and Sr−O distances (r_i) are taken from Tables 3 and 4. For the Sr_2NiIrO_6 oxide, the obtained valences for Ni (+2.45) and Ir (+5.15) suggest the existence of mixed-valence at the B-site. For Sr_2ZnIrO_6, the valence for the Zn cations is +2.39; the excess over the expected 2+ valence indicates that the Zn−O bonds are under compression. This value may also be partially affected by the B-antisite disorder, which is 13% for Sr_2ZnIrO_6, since Ir−O are shorter than Zn−O (Table 4). It is worth noting that in the Ni compound the <Ir−O> bond-lengths are longer, although the unit-cell parameters are rather smaller than in Sr_2ZnIrO_6; this fact confirms the presence of higher percentage of Ir^{6+} (0.52 Å)[15] versus Ir^{5+} (0.57 Å) in the Sr_2ZnIrO_6 sample. For Sr−O bond, valences are 2.05+ and 1.98+ for M = Ni, Zn, respectively, close to those expected.

The $[M/Ir]O_6$ (M = Ni, Zn) octahedral tilt angles can be defined as $\phi = (180 - \omega)/2$, where ω is the Ni/Zn−O−Ir bond angle (Tables 3 and 4). The structure contains alternating $(Ni/Zn)O_6$ and IrO_6 octahedra, tilted in antiphase by ∼7−8° and ∼4−5° along the [100] and [010] directions of the pseudocubic cell, and tilted in phase by ∼8−9° along the [001] direction. This corresponds to the $a^-b^-c^+$ Glazer notation. The O−Ni−O and O−Zn−O bond angles are nearly 90°. The same situation is observed for O−Ir−O angles; thus, the $Ni^{2+/3+}$/Zn^{2+} ions and $Ir^{5+/6+}$ ions are placed in a quasi-regular octahedral environment. This result will be considered in the Discussion of the magnetic results, since the effective magnetic moment for the Ir^{6+} ions can be described as the spin-only value when they are placed in the center of an ideal octahedron.

Low-temperature NPD data were also collected in order to evaluate the possible establishment of a magnetic structure for

Table 1. Unit-Cell, Positional and Displacement Parameters for Sr_2NiIrO_6 Defined in the Monoclinic $P2_1/n$ Space Group at RT, in the Tetragonal $I4/m$ Space Group at 473 and 573 K, and in the Cubic $Fm\bar{3}m$ Space Group at 873 K, Z = 2, from NPD Data

	RT		473 K	573 K		873 K
a (Å)	5.5845(1)	a (Å)	5.55637(8)	5.56628(7)	a (Å)	7.91473(6)
b (Å)	5.5436(1)	c (Å)	7.9091(2)	7.9088(2)		
c (Å)	7.8416(2)	V (Å^3)	241.180(7)	245.040(7)	V (Å^3)	495.802(6)
β (°)	89.979(1)					
V (Å^3)	242.76(1)					
Sr_{4e}(x y z)		**Sr_{4d}(1/4 01/4)**			**Sr_{8c}(1/4 1/4 1/4)**	
x	1.000 (1)	B (Å^2)	1.12(4)	1.50(3)	B (Å^2)	2.27(4)
y	0.011(1)					
z	0.249(2)					
B (Å^2)	0.84(2)					
Ni_{2d}(1/2 0 0)		**Ni_{2a}(0 0 0)**			**Ni_{4a}(0 0 0)**	
Occ. $(Ni/Ir)_{2a}$	0.92(2)/0.08(2)^a					
B (Å^2)	0.81(7)	B (Å^2)	1.6(1)	1.3(2)	B (Å^2)	1.61(9)
Ir_{2c}(1/2 0 1/2)		**Ir_{2b}(0 0 1/2)**			**Ir_{4b}(1/2 1/2 1/2)**	
Occ $(Ir/Ni)_{2b}$	0.92(2)/0.08(2)^a					
B (Å^2)	0.44(6)	B (Å^2)	0.10(9)	0.47(1)	B (Å^2)	0.78(7)
$O1_{4e}$(x y z)		**$O1_{4e}$(0 0 z)**			**$O1_{24e}$(x 0 0)**	
x	0.0443(6)	z	0.250(3)	0.250(5)	x	0.2490(2)
y	0.498(2)	B (Å^2)	1.71(9)	1.7(1)	B (Å^2)	3.06(3)
z	0.247(3)					
B (Å^2)	1.22(4)					
$O2_{4e}$(x y z)		**$O2_{8h}$(x y 0)**				
x	0.747(2)	x	0.223(2)	0.223(3)		
y	0.252(2)	y	0.280(2)	0.277(3)		
z	0.021(2)	B (Å^2)	1.74(6)	1.83(6)		
B (Å^2)	1.37(1)					
Occ						
$O3_{4e}$(x y z)						
x	0.226(1)					
y	0.225(2)					
z	0.974(2)					
B (Å^2)	0.7(1)					
	Reliability Factors					
χ^2	2.08		1.90	2.06		1.70
R_p (%)	2.75		2.84	2.92		2.67
R_{wp} (%)	3.52		3.62	3.79		3.49
R_{exp} (%)	2.44		2.63	2.64		2.68
R_I (%)	2.99		3.10	5.30		3.21

[a] Antisite obtained from XRD data and fixed in the NPD refinement.

Table 2. Unit-Cell, Positional and Displacement Parameters for Sr_2ZnIrO_6 Defined in the Monoclinic $P2_1/n$ Space Group, Z = 2, from NPD Data at RT[a]

	x	y	z	B (Å^2)	Occ
Sr_{4e}	1.0003(8)	0.010(1)	0.245(1)	0.92(2)	1.00
Zn_{2d}	0.5	0	0	0.33(7)	0.87(3)/ 0.13(3)
Ir_{2c}	0.5	0	0.5	0.61(6)	0.87(3)/ 0.13(3)
$O1_{4e}$	0.0484(6)	0.502(1)	0.244(1)	0.997(3)	0.997(3)
$O2_{4e}$	0.213(1)	0.264(1)	0.0225(9)	0.68(5)	0.936(3)
$O3_{4e}$	0.213(1)	0.224(1)	0.9696(9)	1.15(7)	1.00

[a] The unit-cell parameters are a = 5.6216(1) Å, b = 5.5856(1) Å, c = 7.9052(2) Å, β = 89.9902(8)°, and V = 248.22(1) Å^3; the reliability parameters are χ^2 =1.44; R_p (%) = 2.52; R_{wp}(%) = 3.16; R_{exp}(%) = 2.63; R_I (%) = 3.04.

both compounds. Figure 3 shows the difference between the NPD patterns at RT and 2 K. For Sr_2NiIrO_6, a new weak reflection of magnetic origin appears at low temperature at $2\theta \approx 11°$, indicating that the compound exhibits long-range magnetic ordering. However, with one magnetic peak it was not possible to define the propagation vector $\boldsymbol{k}$ and resolve the magnetic structure.

For Sr_2ZnIrO_6, no differences have been observed between both NPD diagrams at 2 K and RT. The absence of magnetic contribution in the low-temperature diffractograms indicates the imperfect establishment of a long-range ordered spin arrangement. Below a certain threshold of long-range coherence, the neutron magnetic Bragg peaks may not have the required intensity to be observed above the background. The imperfect long-range ordering may be due to the formation of a spin-glass state driven by magnetic frustration; the certain degree of antisite disordering (13%) may also be determinant to promote magnetic disordering and frustration.

High-Temperature Evolution of the Crystal Structure of Sr_2NiIrO_6. The XRD patterns collected between RT and 1073 K for Sr_2NiIrO_6 are displayed in Figure S3 (Supporting

Table 3. Main Interatomic Bond Distances (Å) and Selected Angles (deg) for Sr_2NiIrO_6 Determined from NPD Data at RT, 473, 573, and 873 K

RT			473 K	573 K	873 K	
			SrO_{12} Polyhedra			
Sr−O1	2.855 (11)	Sr−O1 (x4)	2.634(7)	2.7832(4)	Sr−O (x12)	2.798(1)
Sr−O1	2.710(11)	Sr−O2 (x4)	2.7782(4)	2.644(11)		
Sr−O1	3.043(6)	Sr−O2 (x4)	2.949(8)	2.943(12)		
Sr−O1	2.544(6)	<Sr−O>	2.787(5)	2.790(9)		
Sr−O2	2.640(16)					
Sr−O2	2.687(16)					
Sr−O2	2.935(17)					
Sr−O2	2.860(17)					
Sr−O3	2.768(16)					
Sr−O3	3.095(15)					
Sr−O3	2.524(15)					
Sr−O3	2.752(14)					
$<Sr-O>_{8\ short}$	2.685(13)					
			NiO_6 Polyhedra			
Ni−O1(x2)	2.00(2)	Ni−O1(x2)	1.98(2)	1.98(4)	Ni−O (x6)	1.971(2)
Ni−O2(x2)	1.971(10)	Ni−O2(x4)	1.99(1)	1.979(17)		
Ni−O3(x2)	1.987(8)	<Ni−O>	1.98(1)	1.97(2)		
<Ni−O>	1.986(12)					
			IrO_6 Polyhedra			
Ir−O1(x2)	1.95(2)	Ir−O1(x2)	1.98(2)	1.98(4)	Ir−O (x6)	1.986(2)
Ir−O2 (x2)	1.978(10)	Ir−O2 (x4)	1.965(11)	1.979(17)		
Ir−O3 (x2)	1.987(9)	<Ir−O>	1.97(1)	1.97(2)		
<Ir−O>	1.972(13)					
			Ni−O−Ir			
Ni−O1−Ir	165.6(1)	Ni −O1−Ir	180.0(1)	180.0(2)	Ni−O−Ir	180.0(6)
ϕ	7.2					
Ni−O2−Ir	170.2(4)	Ni −O2−Ir	167.0(4)	167.7(7)		
ϕ	4.9					
Ni−O3−Ir	163.7(3)					
ϕ	8.2					
O1−Ni−O2	89.7(1)					
O1−Ni−O3	90.6(1)					
O2−Ni−O3	95.9(6)					
O1−Ir−O2	90.2(1)					
O1−Ir−O3	88.9(1)					
O2−Ir−O3	94.0(7)					

Information). A reduction of the splitting of some peaks is observed when the temperature increases, indicating a reduction of the distortion of the unit cell and therefore a possible phase transition. The room temperature phase for Sr_2NiIrO_6 is correctly defined in the monoclinic $P2_1/n$ space group, but at higher temperatures (between 673 and 1073 K) the structure could be accounted for in a cubic cell with $Fm\overline{3}m$ space group.

In the temperature range between 473 and 673 K another characteristic splitting is observed; a shoulder appears in the peak at $2\theta \approx 76.3°$ (marked with an arrow in Figure S2b, Supporting Information), corresponding to the (116) reflection. This shoulder does not satisfy the reflection conditions for either $P2_1/n$ or $Fm\overline{3}m$ space groups, confirming the existence of an intermediate tetragonal phase. The diffraction patterns were indexed satisfactorily with a tetragonal unit-cell in the $I4/m$ space group. Therefore, the thermal evolution of the structure of Sr_2NiIrO_6 shows the presence of two phase transitions following the sequence $P2_1/n \rightarrow I4/m \rightarrow Fm\overline{3}m$ when the temperature increases. A schematic view of the crystal structures corresponding to the different phases is displayed in Figure 4. The temperature dependence of the lattice parameters refined using XRD data at all the measured temperatures is shown in Figure 5, illustrating the increase of the symmetry with the temperature.

A more exhaustive study of the phase transition was carried out in the high resolution D2B instrument (ILL-Grenoble). Figure S4 (Supporting Information) clearly displays a different splitting scheme for the 473 and 573 K NPD diagrams at high angles with respect to the RT pattern and finally a lack of splitting for the 873 K diagram. The crystal structure of the Sr_2NiIrO_6 perovskite was refined in the tetragonal $I4/m$ space group at 473 and 573 K, whereas a cubic $Fm\overline{3}m$ space group was successfully used to define the 873 K structure. Figure 6 shows the goodness of the fits at these temperatures above RT. Figure S5 (Supporting Information) highlights the difference between the 573 and 873 K patterns, clearly showing that the refinement of the structure at 573 K in the cubic $Fm\overline{3}m$ space group does not account for some of the reflections (marked with an arrow in Figure S4b). Tables 1 and 3 summarize the refined parameters using the NPD diffraction data at 473 and 573 K in the tetragonal model and at 873 K in the cubic one.

Table 4. Main Interatomic Bond Distances (Å) and Selected Angles (deg) for Sr_2ZnIrO_6 Determined from NPD Data at RT

RT			
SrO_{12} polyhedra		**IrO_6 polyhedra**	
Sr–O1	2.851(10)	Ir–O1(x2)	1.943(12)
Sr–O1	2.761(10)	Ir–O2 (x2)	1.958(7)
Sr–O1	3.087(6)	Ir–O3 (x2)	1.961(7)
Sr–O1	2.538(6)	<Ir–O>	1.954(9)
Sr–O2	2.684(10)		
Sr–O2	2.667(11)	Zn–O1–Ir	164.3(5)
Sr–O2	2.989(11)	ϕ	7.8
Sr–O2	2.872(11)	Zn–O2–Ir	168.6(3)
Sr–O3	2.760(11)	ϕ	5.7
Sr–O3	3.194(11)	Zn–O3–Ir	160.3(3)
Sr–O3	2.463(11)	ϕ	9.8
Sr–O3	2.818(10)	O1–Zn–O2	89.9(6)
<Sr–O>$_{8\ \mathrm{short}}$	2.693(9)	O1–Zn–O3	90.5(6)
ZnO_6 polyhedra		O2–Zn–O3	95.7/(5)
Zn–O1(x2)	2.047(12)	O1–Ir–O2	91.0(6)
Zn–O2(x2)	2.024(7)	O1–Ir–O3	87.7(6)
Zn–O3(x2)	2.061(7)	O2–Ir–O3	94.0(6)
<Zn–O>	2.044(9)		

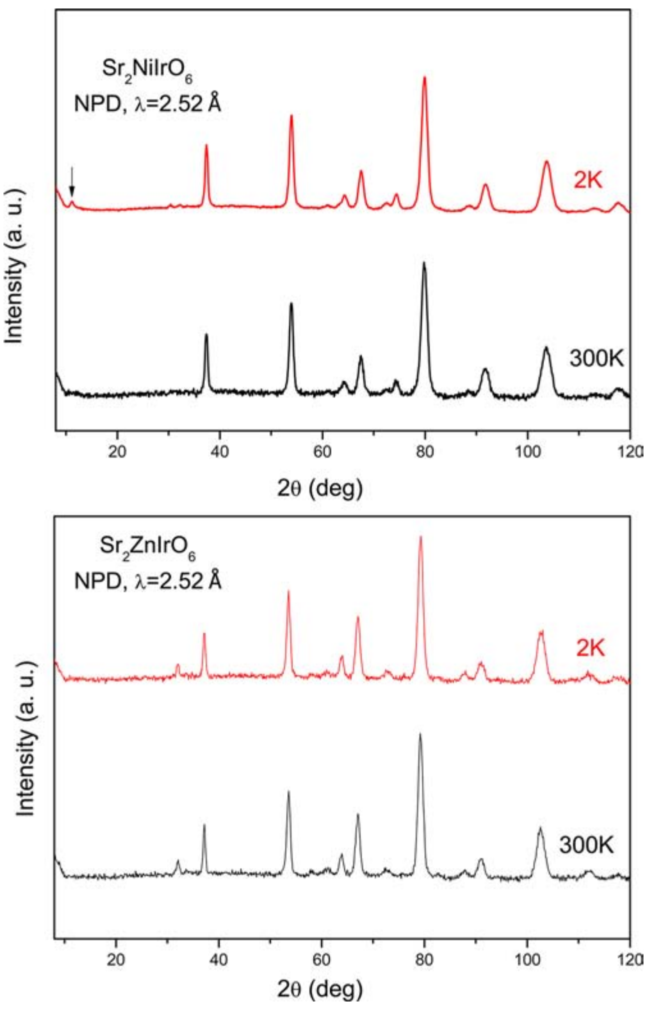

Figure 3. NPD patterns at 2 and 300 K for Sr_2MIrO_6 (M = Ni, Zn) collected at D1B-ILL diffractometer.

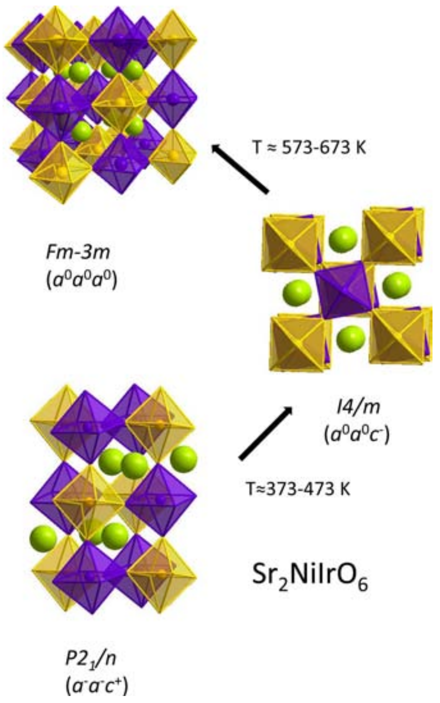

Figure 4. A schematic representation of the crystal structures corresponding to the different phases.

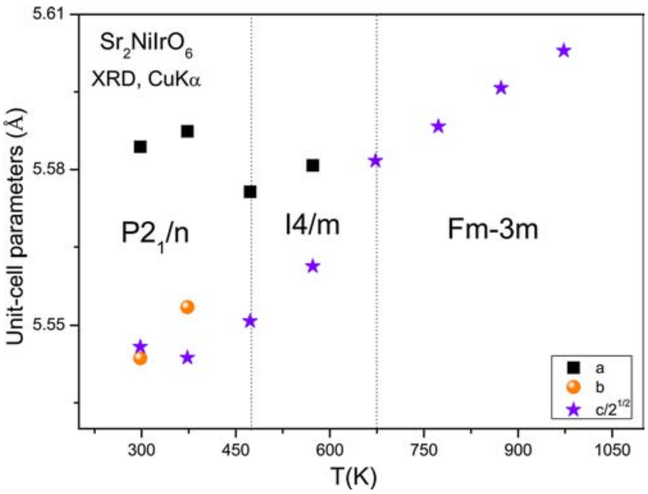

Figure 5. Variation of the unit-cell parameters for Sr_2NiIrO_6 with the temperature.

The tables show the unit-cell and displacement parameters, and the main bond distances and selected angles.

Magnetic Properties. The molar magnetic susceptibility versus temperature curves for the Sr_2NiIrO_6 and Sr_2ZnIrO_6 samples are displayed in Figure 7, suggesting the establishment of antiferromagnetic interactions at Néel temperatures (T_N) around 58 and 46 K, respectively. There is a divergence between ZFC and FC curves below ~150 K for both compounds; this effect corresponds to magnetic irreversibilities which may be related with magnetic frustration or canting of the spins.[32,33] In the Sr_2ZnIrO_6 compound, it appears that there is a second transition responsible for the 150 K anomaly, the origin of which is unclear, although we discard the presence of a second phase, which has not been observed by XRD or NPD data. Below 30 K there is an increase of magnetic susceptibility,

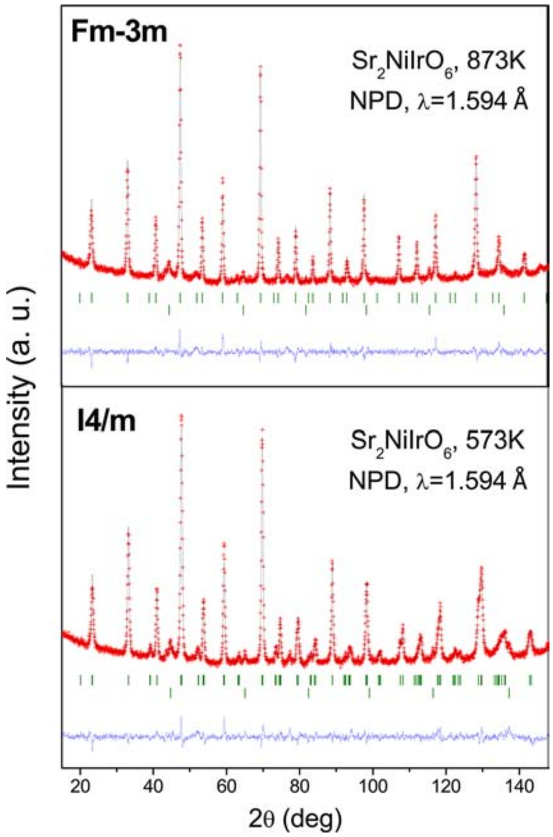

Figure 6. Observed (crosses), calculated (solid line), and difference (bottom) NPD Rietveld profiles for Sr_2NiIrO_6 at 573 and 873 K collected at the high flux D2B-ILL diffractometer. The first series of Bragg reflections correspond to the main perovskite phase and the second corresponds to the vanadium from the sample holder.

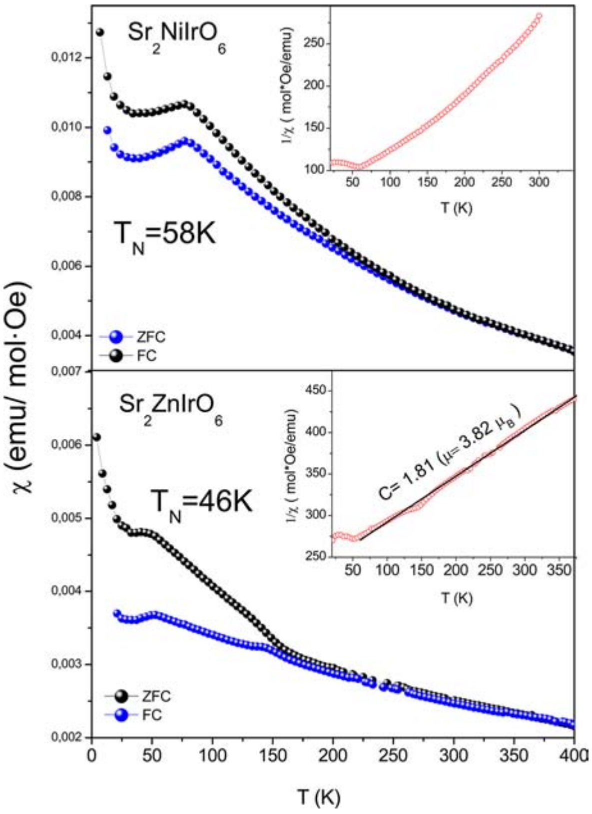

Figure 7. Temperature dependence of the *dc* magnetic susceptibility for the Sr_2MIrO_6 (M = Ni, Zn) perovskites, measured under a 0.1 T magnetic field. The inset shows the reciprocal ZFC susceptibility versus temperature.

which is a very frequently observed feature corresponding to a paramagnetic tail, coming from the imperfect long-range ordering of the antiferromagnetic material, leaving some isolated patches of nonordered atoms which follow the usual thermal dependence of paramagnetic substances.

As shown in the inset of Figure 7, for M = Ni the reciprocal susceptibility data do not obey the Curie−Weiss Law above T_N, which is probably due to the dependence of the effective moment of Ir^{5+} with temperature, depending on the degree of spin−orbit coupling.[18,34] For M = Zn, the linear fit gives a value of the experimental paramagnetic moment of $\mu_{eff} = 3.82\ \mu_B$ with a negative values of Weiss temperature (−430 K), suggesting the presence of antiferromagnetic interactions in this compound.

Moreover, in Sr_2ZnIrO_6, where iridium is the only magnetic ion, the experimental value corresponds to three unpaired electrons ($t^3_{2g}e_g^0$) and confirms the stabilization of Ir^{6+}. According to the expression $\mu_{eff} = \mu_{spin\text{-}only}$ $(1 - 4\lambda/10Dq)$, where λ is the spin−orbit coupling constant, the effective magnetic moment, μ_{eff}, of d^3cations (ground term $^4A_{2g}$) is expected to be reduced from the spin-only value by the factor $(1 - 4\lambda/10Dq)$.[15,35] However, the calculated value of $\mu_{spin\text{-}only}$ (Ir^{6+}) = 3.87 μ_B is in reasonable agreement with the experimental value. This t^3_{2g} electron configuration in the ideal octahedral crystal field has a nearly null orbital angular momentum.

The magnetization vs magnetic field curves, measured at 4 and 300 K (Figure 8) present an almost linear behavior confirming the presence of antiferromagnetic interactions. The inset plots of Figure 8 show a subtle magnetic hysteresis in both compounds indicating weak ferromagnetic interactions possibly due to the canting of the spins.

X-ray Absorption Measurements. *3d Row K-Edge XAS: Ni and Zn.* X-ray absorption spectroscopy studies have been useful to clarify the oxidation states in both materials. The Ni−K near-edge features are due to transitions from the 1s to 4p states superimposed on an underlying step-feature due to the onset of continuum transitions. Multiple 4p features associated with different 3d configurations and with differing orbital orientations make the interpretation of the near edge features nontrivial.[36−38] Nevertheless, the systematic energy shifts in the K-edges, upon doping/chemical changes, and the variation of feature intensities can serve as indicators of charge states in 3d transition metal compounds.

The Ni−K edge of La_2TiNiO_6, recorded as a reference (see the central portion of Figure 9a), is typical of Ni^{2+} 3d-row perovskite-based materials. By comparison, the Ni^{3+} standard $LaNiO_3$ spectrum has a broader main peak and is chemically shifted to higher energy. The intensity and structure (an intense peak with a higher energy shoulder) for the Sr_2NiIrO_6 compound spectra are intermediate to those of the Ni^{2+} and Ni^{3+}standards, since the main edge peak of the Ir-compound is shifted to higher energy relative to the Ni^{2+} perovskite standard.

Referring to Figure 9b, the Zn−K edge spectra of La_2TiZnO_6 and Sr_2ZnIrO_6 are compared with an energy scale equivalent to that in Figure 9a. Despite the Zn^{2+} state for both of these compounds, the Ir-compound peak-feature is shifted up in energy relative to the Ti-compound. Indeed, the results of the

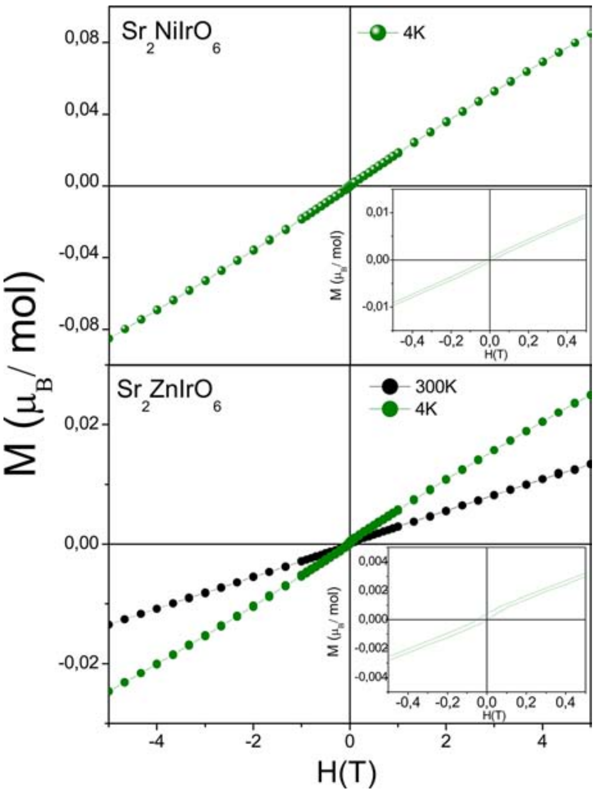

Figure 8. Magnetization versus magnetic field isotherms of Sr_2MIrO_6 (M = Ni, Zn) at 300 K and 4 K measured under a magnetic field ranging from −5 to 5 T.

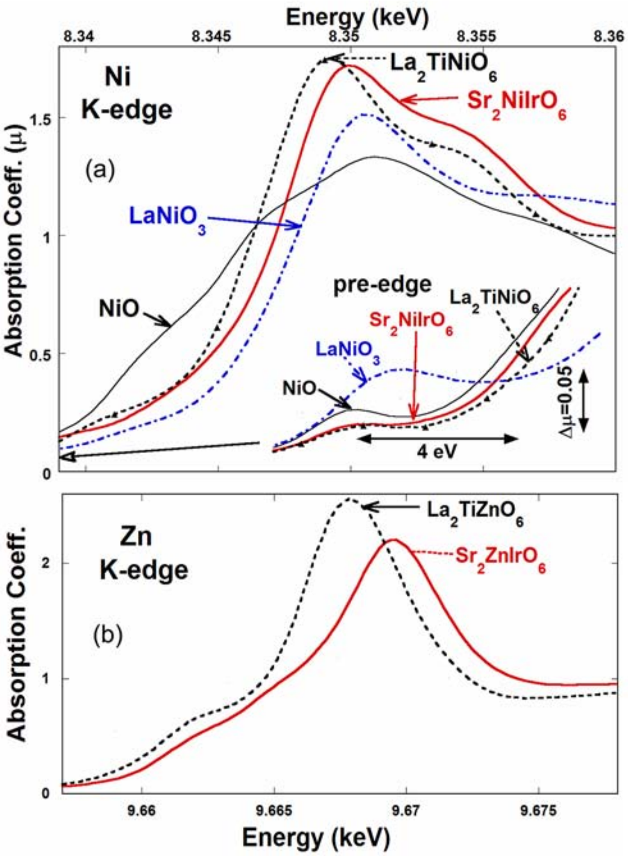

Figure 9. (a) Ni−K edges of Sr_2NiIrO_6 compared with the Ni^{3+}, $LaNiO_3$ and Ni^{2+} NiO and Sr_2TiNiO_6 octahedrally coordinated standard spectra. Inset lower right: An expanded view of the pre-edges region of these Ni spectra. (b) The Zn−K edges of La_2ZnIrO_6 and the Zn^{2+} standard Sr_2TiZnO_6.

neutron study also suggest a Zn valence above the divalent state, which is unphysical and may be related to covalency effects.

The pre-edge features of the Ni-compounds, presented on enlarged absorption coefficient and energy scales in the lower right inset of Figure 9a, can be used to corroborate the substantial amount of Ni^{2+} present in Sr_2NiIrO_6. The pre-edge features at the K-edges of 3d transition metal compounds are due to quadrupole-allowed transitions into final *d*-states or into hybridization-allowed dipole transitions into d/ligand-p states and are shifted below the main edge by the final state d-electron/core-hole Coulomb interaction.[36−38] The structure of these pre-edge features varies with the d-state structure in the different valence states. Moreover with increasing valence (decreasing d-orbital occupation) the integral area and centrum-energy of the pre-edge features typically increase. In the left upper inset of Figure 9a, the pre-edge feature of Sr_2NiIrO_6 can be seen to have a substantially lower intensity and energy (like the NiO and La_2TiNiO_6 Ni^{2+}-standards) relative to the $LaNiO_3$ Ni^{3+}-standard. Thus, the main- and pre-edge Ni−K edge results mutually support the predominant Ni^{2+}contents of Sr_2NiIrO_6.

Having the two M = Ni and Zn examples of $Sr_2M^{2+}IrO_6$ materials, it is useful to consider an appropriate M^{3+} example for comparison. In Figure S6, Supporting Information, the Fe K-edge of Sr_2FeIrO_6 is shown along with a number of Fe standard compounds. In analogy to that described above, the Fe^{2+} standard spectra (FeO and $LiFePO_4$) lie much lower in energy relative to the Fe^{3+} standard spectrum ($LaSrFeO_4$). The spectral evolution toward a ∼Fe^{4+} state (see $SrFeO_{3-\delta}$) involves a more subtle energy shift but a substantial decrease in the main peak intensity at the edge. The similarity in chemical shift energy and edge feature structure to that of $LaSrFeO_4$ motivates a Fe^{3+} identification for the Sr_2FeIrO_6 compound. As mentioned above, the Fe−K pre-edge region provides a useful contribution for the Fe valence state identification. An expanded view of the pre-edges of the Fe−K edge spectra are shown in the inset of Figure S6. The strong similarity in energy and intensity of Sr_2FeIrO_6 and $LaSrFeO_4$ pre-edges, coupled with the strong disparities compared to the pre-edge spectra of the higher and lower valence standards, are clear in the inset. Thus, the pre-edge spectra confirm the main-edge Fe^{3+}-identification for Sr_2FeIrO_6.

Ir L_3-edge XAS. The $L_{2,3}$ edges of transition metal (T) compounds manifest very intense "white line" (WL) features due to dipole transitions into final d states. In an octahedral ligand field, the 10 d states are split into a t_{2g} state lying below e_g multiplets with respective six- and 4-fold degeneracies. In many high-hole (low-electron) count octahedral T-4d and -5d compounds, separate t_{2g} and e_g related features can be discerned in their $L_{2,3}$ edge[38,39] spectra. In such materials, the relative intensities of the separate t_{2g} and e_g features can visually reflect hole (electron)[38,39] count variations. In addition, the increasing chemical shift of the WL features to higher energy with increasing T-*d* hole count (increasing valence) is also observed. Here the reflection of the varying Ir-valences in the Ir-L_3 edges of a series of compounds will be considered. Figure 10 shows the Ir-L_3 edges of elemental-Ir, IrO_2 and the double

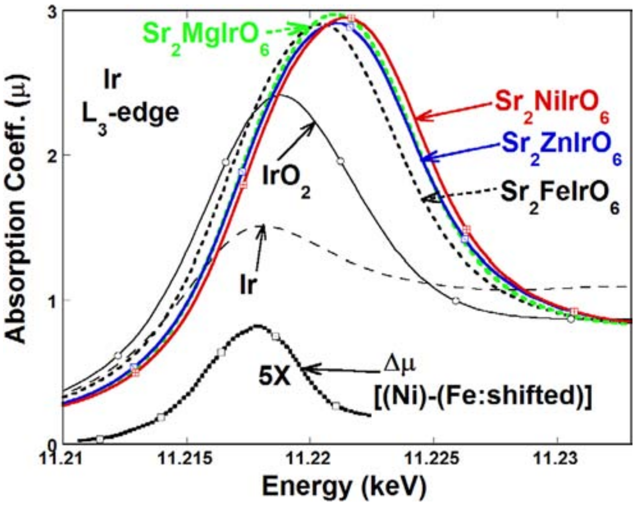

Figure 10. The Ir-L_3 edges of Sr_2MIrO_6 with M = Mg, Fe, Ni, and Zn along with those of elemental-Ir and IrO_2. Plotted on a 5-fold enlarged vertical scale, at the bottom of the figure is the spectral difference $\Delta\mu$. $\Delta\mu$ was obtained by first shifting the M = Fe spectrum up in energy until it coincided with the M = Ni spectrum on the high energy side of the WL feature, and then subtracting the shifted-Fe spectrum from the Ni spectrum.

perovskites Sr_2MIrO_6 with M = Mg, Fe, Ni, and Zn. The large chemical shift and increase in WL spectral weight between the IrO_2, Ir^{4+} standard and the Sr_2MIrO_6 double perovskites should be noted first and foremost. This is qualitatively consistent with the formal Ir^{5+} and Ir^{6+} states of the latter. Comparing the Sr_2MIrO_6 spectra, one notes that the M = Fe^{3+}, Ir^{5+}-spectrum is noticeably shifted to lower energy with respect to the M = Mg, Zn, and Ni spectra. The M = Mg^{2+} and Zn^{2+} spectra lie quite close and M = Ni^{2+} has a slightly higher energy shift. Thus, the signature of the formal Ir^{6+} character in the M = Mg, Zn, and Ni spectra (relative to the M = Fe^{3+}, Ir^{5+}-spectrum) is clear but not large.

In order to highlight the modest Ir^{5+}-Ir^{6+} spectral changes, the M = Fe^{3+} spectrum has been shifted up in energy until it coincided approximately with the M = Ni^{2+} spectrum in the high energy side of the WL feature. This is the energy range where the empty states of the e_g orbitals should have a similar spectral structure. A spline fit interpolation of the shifted M = Fe^{3+} spectrum was then subtracted from the M = Ni^{2+} spectrum to extract the $\Delta\mu$ difference spectrum plotted on a 5-fold enlarged vertical scale in the inset of Figure 10. Here the $\Delta\mu$ difference spectrum is intended to illustrate the distribution of excess t_{2g} hole states on the rising edge of the WL feature of the M = Ni compound. The $M^{2+}Ir^{6+}$ compounds all have such an excess intensity on the rising edge-shoulder of the WL; however, these shoulder features are rather subtle.

■ DISCUSSION

X-ray powder diffraction and neutron powder diffraction studies show that Sr_2NiIrO_6 and Sr_2ZnIrO_6 crystallize with the monoclinic $P2_1/n$ superstructure at room temperature. The structure consists of a tridimensional network of Ni/ZnO_6 and IrO_6 alternating octahedra with 1:1 rock-salt ordering. For the Sr_2NiIrO_6 perovskite, the size and the charge difference between both cations as driving force for the long-range ordering is reinforced by the covalence of Ir—O bonds, since the anion polarization is maximum for asymmetric B—O—B′ linkages rather than for symmetric B—O—B linkages. For the Zn perovskite, the difference in the size and charge between both cations is even higher; thus, the Zn/Ir long-range ordering is also possible according to the Anderson et al.[40] criterion. Table 2 shows that ZnO_6 octahedron is larger than IrO_6 octahedron, which agrees with the difference of ionic radii.[22]

Results of the bond valence analysis according to the Brown model[30] (Tables 3 and 4) confirm the presence of mixed-valence at the B-site: for Sr_2NiIrO_6 we found 55%−45% for Ni^{2+}−Ni^{3+} and 85%−15% for Ir^{5+}−Ir^{6+}. According to the refinement of the oxygen occupancy factor, in the $Sr_2ZnIrO_{5.87(1)}$ compound, the valence of the iridium cations presents a value of +5.74, which means a percentage of 26% of Ir^{5+} and 74% of Ir^{6+}. This is in good agreement with the experimental Ir−O distance, slightly longer than the corresponding to Ir^{6+}−O. Those features have been mostly confirmed in the XANES experiments, which perfectly complement the structural findings obtained from NPD data.

Two phase transitions are observed in Sr_2NiIrO_6. At room temperature, the structure can be described, in the framework of rigid octahedral rotations, with the $a^-a^-c^+$ Glazer notation. At 473 K, it is tetragonal, $I4/m$ space group, and it is defined as a result of a single antiphase octahedral tilting along the c axis, corresponding to the $a^0a^0c^-$ Glazer notation. Beyond 673 K, it can be refined as cubic, $Fm\bar{3}m$, without octahedral tilting, as described by the $a^0a^0c^0$ Glazer notation. The first phase transition corresponds, thus, to the reduction of two tilts in "anti-phase" in the a and b directions, in addition with a change from "in-phase" to "anti-phase" in the c direction, as shown in Figure 4. In the second phase transition, the suppression of this rotation along the c axis leads to an untilted cubic symmetry.

The magnetic measurements suggest the establishment of antiferromagnetic interactions at Néel temperatures (T_N) around 58 and 46 K, respectively. The divergence of the field-cooled and zero-field-cooled curves at low temperature suggests the existence of geometrical frustration in these materials. Magnetic frustration is a common phenomenon in antiferromagnetic double perovskites, and it is attributed to the competition between different magnetic interactions. When frustration arises from the geometry or topology of the lattice, it is named geometric frustration. It occurs in Kagome lattices, based in an equilateral triangle, and also in three-dimensional systems, such as face centered cubic (fcc) compounds and pyrochlores. In double perovskites, the rock-salt sublattice consists of the interpenetrating B and B′ fcc sublattices, and thus, these systems may show magnetic frustration.[41,42]

A frustration index f_{frus}, defined as $f_{frus} = |\theta_{Weiss}|/T_N$, is normally used as a measure of the degree of frustration in a magnetic material.[43] Usually for geometrically frustrated materials $f_{frus} > 10$. The f_{frus} for Sr_2ZnIrO_6 is ∼9.5, confirming the presence of magnetic frustration in our compound. This effect may also account for the absence of long-range magnetic ordering observed by low temperature neutron diffraction.

■ CONCLUSION

In conclusion, double perovskites 3d-5d containing Ir^{5+}−Ir^{6+}, with the formulas Sr_2MIrO_6 (M = Ni, Zn), have been prepared from citrate precursors under oxidizing conditions. XRD and NPD studies confirm that these oxides present an ordered arrangement of the B-site cations at room temperature and that its structure at RT can be described with the $P2_1/n$ space group. A XANES study gives a complementary insight of the oxidation states of 3d and Ir ions. The study of the temperature dependence of the crystal structure shows the presence of two phase transitions for Sr_2NiIrO_6 compound in the 373−673 K interval. The susceptibility measurements suggest the establishment of antiferromagnetic interactions at Néel temperatures (T_N) around 58 and 46 K, respectively. The divergence in the field-cooled and zero-field-cooled curves at low temperature may indicate the existence of geometrical frustration in these materials, which accounts for the absence of long-range magnetic ordering observed by low temperature neutron diffraction for M = Zn.

■ ASSOCIATED CONTENT

Ⓢ Supporting Information

Structural analysis; Figures S1−S6. This material is available free of charge via the Internet at http://pubs.acs.org.

■ AUTHOR INFORMATION

Corresponding Author

*E-mail: paula.kayser@icmm.csic.es.

Notes

The authors declare no competing financial interest.

■ ACKNOWLEDGMENTS

We acknowledge the financial support of the Spanish Ministry of Science and Technology to the project MAT2010-16404 and of the Comunidad de Madrid to the Project S2009PPQ-1551. We thank Dr. M. García-Hernández for the magnetic measurements, and we are grateful to the Institut Laue-Langevin (ILL) for making all facilities available. Use of the National Synchrotron Light Source, Brookhaven National Laboratory, was supported by the U.S. Department of Energy, Office of Science, Office of Basic Energy Sciences, under Contract No. DE-AC02-98CH10886.

■ REFERENCES

(1) Clancy, J. P.; Chen, N.; Kim, C. Y.; Chen, W. F.; Plumb, K. W.; Jeon, B. C.; Noh, T. W.; Kim, Y.-J. *Phys. Rev. B* **2012**, *86*, 195131.
(2) Moon, S. J.; Kim, M. W.; Kim, K. W.; Lee, Y. S.; Kim, J.-Y.; Park, J.-H.; Kim, B. J.; Oh, S.-J.; Nakatsuji, S.; Maeno, Y.; Nagai, I.; Ikeda, S. I.; Cao, G.; Noh, T. W. *Phys. Rev. B* **2006**, *74*, 113104.
(3) Bremholm, M.; Dutton, S. E.; Stephens, P. W.; Cava, R. J. *J. Solid State Chem.* **2011**, *184*, 601.
(4) Pesin, D. A.; Leon Balents. *Nat. Phys.* **2010**, *6*, 376.
(5) Witczak-Krempa, W.; Kim, Y. B. *Phys. Rev. B* **2012**, *85*, 045124.
(6) Longo, J. M.; Kafalas, J. A.; Arnott, R. J. *Solid State Chem.* **1971**, *3*, 174.
(7) Zhao, J. G.; Yang, L. X.; Yu, Y.; Li, F. Y.; Yu, R. C.; Fang, Z.; Chen, L. C.; Jina, C. Q. *J. Appl. Phys.* **2008**, *103*, 103706.
(8) Lindsay, R.; Strange, W.; Chamberland, B. L.; Moyer, R. O., Jr. *Solid State Commun.* **1993**, *86*, 759.
(9) Cheng, J.-G.; Zhou, J.-S.; Alonso, J. A.; Goodenough, J. B.; Sui, Y.; Matsubayashi, K.; Uwatoko, Y. *Phys. Rev. B* **2009**, *80*, 104430.
(10) Laguna-Marco, M. A.; Haskel, D.; Souza-Neto, N.; Lang, J. C.; Krishnamurthy, V. V.; Chikara, S.; Cao, G.; van Veenendaal, M. *Phys. Rev. Lett.* **2010**, *105*, 216407.
(11) Kobayashi, K. I.; Kimora, T.; Sawada, H.; Terakura, K.; Tokura, Y. *Nature* **1998**, *395*, 677.
(12) Lee, K.-W.; Pickett, W. E. *Phys. Rev. B* **2008**, *77*, 115101.
(13) Kato, H.; Okuda, T.; Okimoto, Y.; Tomioka, Y.; Takenoya, Y.; Ohkubo, A.; Kawasaki, M.; Tokura, Y. *Appl. Phys. Lett.* **2002**, *81*, 328.
(14) Mandal, T. K.; Felser, C.; Greenblatt, M.; Kubler, J. *Phys. Rev. B* **2008**, *78*, 134431.
(15) Jung, D. Y.; Demazeau, G. *J. Solid State Chem.* **1995**, *115*, 447.
(16) Battle, P. D.; Blake, G. R.; Gibb, T. C.; Vente, J. F. *J. Solid State Chem.* **1999**, *145*, 541.
(17) Mikhailova, D.; Narayanan, N.; Gruner, W.; Voss, A.; Senyshyn, A.; Trots, D. M.; Fuess, H.; Ehrenberg, H. *Inorg. Chem.* **2010**, *49*, 10348.
(18) Wakeshima, M.; Harada, D.; Hinatsu, Y. *J. Alloys Compd.* **1999**, *287*, 130.
(19) Ilyas Qasim; Brendan, J.; Kennedy; Maxim Avdeev. *J. Mater. Chem. A* **2013**, *1*, 3127.
(20) Rietveld, H M *J. Appl. Crystallogr.* **1969**, *2*, 65.
(21) Rodríguez-Carvajal. *J. Phys. B* **1993**, *192*, 55.
(22) Shannon, R. D. *Acta Crystallogr., Sect. A* **1976**, *32*, 751.
(23) Martínez-Lope, M. J.; Alonso, J. A.; Casais, M. T. *Eur. J. Inorg. Chem.* **2003**, 2839.
(24) RetuertoM.Martinez-LopeM. J.Garcia-HernandezM.Fernandez-DiazM. T.AlonsoJ. A.*Eur. J. Inorg. Chem.*2008588
(25) Pinacca, R. M.; Viola, M. C.; Pedregosa, J. C.; Martínez-Lope, M. J.; Carbonio, R. E.; Alonso, J. A. *J. Solid State Chem.* **2007**, *180*, 1582.
(26) Alonso, J. A.; Martínez-Lope, M. J.; Casais, M. T.; Aranda, M. A. G.; Fernández, M. T. *J. Am. Chem. Soc.* **1999**, *121*, 4754.
(27) Choy, J. H.; Kim, D. K.; Hwang, S. H.; Demazeau, G.; Jung, D. Y. *J. Am. Chem. Soc.* **1995**, *117*, 8557.
(28) Jung., D. Y.; Gravereau, P.; Demazeau, G. *Eur. J. Solid State Inorg. Chem.* **1993**, *30*, 1025.
(29) Brown, I. D. *Structure and Bonding in Crystals*; O'Keefe, M., Navrotsky, A., Eds.; New York: Academic Press, 1981; Vol. 2; p 1.
(30) Brown, I. D. *Z. Kristallogr.* **1992**, *199*, 255.
(31) Brese, N. E.; O'Keefe, M. *Acta Crystallogr. Sect. B* **1991**, *47*, 192.
(32) Powell, V.; Gore, J. G.; Battle, P. D. *J. Alloys Compd.* **1993**, *201*, 73.
(33) Kim, S. H.; Battle, P. D. *J. Magnetism Magnetic Mater.* **1999**, *123*, 273.
(34) Walewski, M.; Buffat, B.; Demazeau, G.; Wagner, F.; Pouchard, M.; Hagenmuller, P. *Mater. Res. Bull.* **1983**, *18*, 881.
(35) Izumiyama, Y.; Doi, Y.; Wakeshima, M.; Hinatsu, Y.; Shimojo, Y.; Morii, Y. *J. Phys.: Condens. Matter* **2001**, *13*, 1303.
(36) Sahiner, A.; Croft, M.; Gua, S.; Perez, I.; Zhang, Z.; Greenblatt, M.; Metcalf, P.; Johns, H.; Liang, G. *Phys. Rev. B* **1995**, *51*, 5879.
(37) Sahiner, A.; Croft, M.; Zhang, Z.; Greenblatt, M.; Perez, I.; Metcalf, P.; Jhans, H.; Liang, G.; Jeon, Y. *Phys. Rev.B* **1996**, *53*, 9745.
(38) Whaley, L.; Lobanov, M.; Sheptyakov, D.; Croft, M.; Ramanujachary, K.; Lofland, S.; Stephens, P.; Her, J.-H.; Van Tendeloo, G.; Rossell, M.; Greenblatt, M. *Chem. Mater.* **2006**, *18*, 3448.
(39) Popov, G.; Greenblatt, M.; Croft, M. *Phys. Rev.* **2003**, *B67*, 024406.
(40) Anderson, M. T.; Greenwood, K. B.; Taylor, G. A.; Poeppelmeier, K. R. *Prog. Solid State Chem.* **1993**, *22*, 197.
(41) Bos, J.-W. G.; Attfield, J. P. *Phys. Rev. B* **2004**, *51* (70), 174434.
(42) Karunadasa, H.; Huang, Q.; Ueland, B. G.; Schiffer, P.; Cava, R. J. *Proc. Natl. Acad. Sci. U. S. A.* **2003**, *100*, 8097.
(43) Wiebe, C. R.; Greedan, J. E.; Luke, G. M.; Gardner, J. S. *Phys. Rev. B* **2002**, *65*, 144413.